Three-Dimensional Contact Analysis of Elastic-Plastic Layered Media With Fractal Surface Topographies

K. Komvopoulos, Professor, Mem. ASME
N. Ye, Graduate Student
Department of Mechanical Engineering
University of California
Berkeley, CA 94720

Abstract

Three-dimensional rough surfaces were generated using a modified two-variable Weierstrass-Mandelbrot function with fractal parameters determined from real surface images. The number and size of truncated asperities were assumed to follow power-law relations. A finite element model of a rigid sphere in normal contact with a semi-infinite elastic-plastic homogeneous medium was used to obtain a constitutive relation between the mean contact pressure, real contact area, and corresponding representative strain. The contact model was extended to layered media by modifying the constitutive equation of the homogeneous medium to include the effects of the mechanical properties of the layer and substrate materials and the layer thickness. Finite element simulations of an elastic-plastic layered medium indented by a rigid sphere validated the correctness of the modified contact model. Numerical results for the contact load and real contact area are presented for real surface topographies resembling those of magnetic recording heads and smooth rigid disks. The model yields insight into the evolution of elastic, elastic-plastic, and fully plastic deformation at the contact interface in terms of the maximum local surface interference. The dependence of the contact load and real contact area on the fractal parameters and the carbon overcoat thickness is interpreted in light of simulation results obtained for a tri-pad

picoslider in contact with a smooth thin-film hard disk.

1. Introduction

Understanding of contact between rough surfaces is important in many engineering fields and has direct implications on the product performance of various leading-edge technologies, such as computer hard disk drives and microelectromechanical systems. In order to obtain analytical solutions for the subsurface stress and strain fields, the contact pressure and real contact area must be determined first. Although various analytical methods for obtaining such information have been reported [1-4], these methods are fairly complex and programming is often inhibited by convergence problems.

In view of advances in sophisticated numerical methods, such as the finite element method, and remarkable enhancements in computational capabilities, such shortcomings were overcome in more recent contact mechanics studies. Johnson [5] analyzed the indentation response of elastic-plastic solids and reported the successive occurrence of elastic, elastic-plastic, and fully plastic deformation with increasing indentation depth. Mesarovic and Fleck [6] obtained deformation maps for strain-hardening homogeneous media indented by a rigid sphere and showed that the fully plastic region comprises two regimes: a similarity regime for small contact sizes and a finite-deformation plasticity regime for large contact sizes. Finite element simulations of indented layered media by Kennedy and Ling [7], Van der Zwaag and Field [8], Komvopoulos [9,10], and Tian and Saka [11] have shown a pronounced effect of the layer thickness and mechanical properties on the deformation behavior. Results from a three-dimensional finite element analysis of a rigid sphere indenting or sliding over an elastic-plastic layered medium performed by Kral and Komvopoulos [12] have illustrated the effects of the layer material properties, coefficient of friction, and normal load on the sliding and residual stress fields and the

forward plastic flow at the contact region.

Although significant insight into the mechanics of contacting solids has been obtained from the aforementioned analytical and numerical studies, the information obtained can only be related to the macroscopic deformation behavior because of the assumed ideally smooth surfaces. However, real surface topographies comprise geometrical features spanning a wide range of length scales, i.e., a similar topography is obtained after arbitrary magnification. Knowledge of the local deformation behavior at surface summits (asperity microcontacts) where actual contact occurs is of great importance to the durability of many engineering devices. One of the primitive contact models that accounts for roughness effects is attributed to Greenwood and Williamson [13] who developed an asperity deformation criterion based on a probabilistic mathematical model of the surface height distribution. It was assumed that the asperity heights follow a normal distribution function, while the radii of curvature and lateral distribution of the asperities are invariant. Larsson et al. [14] examined theoretically the initial flattening of rough surfaces and reported a linear contact area-load relation for a perfectly plastic material and an exponential asperity height distribution, and a nonlinear contact pressure-area relation for a normal asperity height distribution and strain hardening material behavior.

However, most engineering surfaces exhibit random and multi-scale topographies that can be characterized by fractal geometry [15,16]. The advantages of using fractal geometry for surface description include scale invariance (i.e., independence of the measurements on the instrument resolution and the sample length) and self-affinity (i.e., as the magnification increases finer details of surface features similar to the original profile emerge). These important properties of fractal geometry make it appropriate for characterizing engineering surfaces over a wide range of length scales. The paper that, presumably, brought fractals to the attention of the engineering community is that of Majumdar and Tien

[17] who examined the roughness of steel surfaces and a textured magnetic thin-film disk and observed statistically similar surface images at various magnifications. It was reported that the surface roughness could be characterized by a Weierstrass-Mandelbrot (W-M) fractal function [16,18]. One of the first contact analysis to use a fractal description for the surface topography is that of Majumdar and Bhushan [19]. They obtained a relation for the real contact area and estimated the critical asperity size demarcating the transition from elastic to fully plastic asperity deformation. It was shown that small asperities deform plastically while large asperities deform elastically, a radically different result from what is predicted from the model of Greenwood and Williamson [13]. Blackmore and Zhou [20,21] introduced a fractal-based functional model for anisotropic rough surfaces and argued that a very extensive class of engineering surfaces possesses surface height distributions that depend in significant ways on fundamental fractal parameters.

Ciavarella et al. [22] considered normal contact between an elastic half-space and a rigid fractal surface, whose profile was defined by a Weierstrass series, and observed that, at large wavelength numbers, the contact area exhibited limiting power-law fractal behavior. Wang and Komvopoulos [23-25] developed a fractal contact theory for the temperature rise on elastic-plastic rough surfaces sliding in the slow and fast speed regimes and showed that a continuous transition from elastic to fully plastic deformation (i.e., elastic-plastic deformation) occurs at asperity microcontacts. It was also indicated that the elastic-plastic regime could be significantly broad, depending on the material properties and fractal dimensions of the sliding surfaces [24]. More recently, Yan and Komvopoulos [26] introduced a three-dimensional fractal mechanics theory for elastic-plastic surfaces in normal contact and obtained numerical results for the average contact pressure and real contact area in terms of the mean surface separation distance.

Despite important information about contact deformation at smooth and rough surfaces obtained from the previous studies, a comprehensive contact analysis of elastic-plastic layered media exhibiting rough surface topographies (characterized by fractal geometry) has not been performed yet. Thus, the main objective of the present study was to bridge the gap between contact mechanics applicable to a single asperity microcontact and interactions occurring at multi-scale contact interfaces of layered media possessing realistic surface topographies. To accomplish this goal, a finite element model was developed in order to obtain relations between the mean contact pressure and real contact area for a single spherical asperity indenting an elastic-plastic homogeneous medium in terms of a representative strain, which is a function of the surface interference distance and the mechanical properties of the medium. The constitutive model was extended to layered media to account for the mechanical properties of the layer and substrate materials and the effect of the layer thickness. For multi-scale surface description, three-dimensional fractal geometry was used to characterize the surface topography. The effects of the fractal parameters and layer thickness on the contact load and real contact area are interpreted in light of results obtained for a tri-pad picoslider in contact with a smooth thin-film disk.

2. Surface Modeling

The topographies of engineering surfaces have been traditionally quantified in terms of the height variance, slope, and curvature of surface summits. The values of these parameters depend on the instrument resolution and the sample length. However, a realistic multi-scale roughness description can only be accomplished by using scale-independent parameters, such as the scale-invariant parameters used in fractal geometry [15,16]. A three-dimensional fractal surface topography can be generated using a modified (truncated) two-variable W-M function [15,16] that can be written as [26]

$$z(x,y) = L\left(\frac{G}{L}\right)^{D-2}\left(\frac{\ln g}{M}\right)^{1/2}\sum_{m=1}^{M}\sum_{n=0}^{n_{\max}} g^{(D-3)n}\left\{\cos f_{m,n} - \cos\left[\frac{2\pi g^{n}\left(x^2+y^2\right)^{1/2}}{L}\cos\left(\tan^{-1}\left(\frac{y}{x}\right) - \frac{\pi m}{M}\right) + f_{m,n}\right]\right\}, \quad (1)$$

where L is the sample length, G is the fractal roughness, D is the fractal dimension ($2 < D < 3$), g ($g > 1$) is a scaling parameter, M is the number of superposed ridges used to construct the surfaces, n is a frequency index, with $n_{\max} = \text{int}\left[\log(L/L_s)/\log g\right]$ representing the upper limit of n, where L_s is the cut-off length, and $\phi_{m,n}$ is a random phase. The scaling parameter g controls the density of frequencies in the surface profile. Based on surface flatness and frequency distribution density considerations, $g = 1.5$ [26]. For a truncated series (i.e., starting at $n = 0$ rather than $n = -\infty$ (Eq. (1)), the scaling property is approximate, i.e., scaling is satisfied only to within a small additive term [27]. Thus, the surface function given by Eq. (1) possesses a scale-invariant (fractal) behavior [18] only within a finite range of length scales, outside of which, the surface topography can be represented by a deterministic function [24]. In practice, the smallest length corresponds to the instrument resolution and the upper length to the length of the profile. Because frequencies outside the range determined by the lower and upper wavelengths do not contribute to the observed profile, self-similarity is satisfied at all scales only approximately [28]. The fractal roughness G is a height scaling parameter independent of frequency (within the scale range that fractal power-law behavior is observable). The magnitude of the fractal dimension D determines the contribution of high and low frequency components in the surface function $z(x,y)$. Thus, high values of D indicate that high-frequency components are more dominant than low-frequency components in the surface topography profile. The surface height function given by Eq. (1) is continuous, non-differentiable, scale-invariant (in the range determined by the upper and lower wavelengths used in the truncated series), and self-affine (asymptotically self-affine according to the analysis of Blackmore and Zhou [20,21]). The latter implies that as the surface is repeatedly magnified, more and more surface

features appear and the magnified image shows a close resemblance to that of the original surface obtained at a different scale. These properties make the function given by Eq. (1) suitable for constructing surfaces possessing topographies closely resembling the actual surfaces from which the fractal parameters *D* and *G* were determined experimentally.

3. Elastic-Plastic Constitutive Model

A system of two contacting rough surfaces can be replaced by an equivalent system of a flat deformable surface with an effective elastic modulus $E^* = \left[\left(1-\nu_1^2\right)/E_1 + \left(1-\nu_2^2\right)/E_2\right]^{-1}$, where ν_1, ν_2, and E_1, E_2 are the Poisson's ratios and elastic moduli of the two interacting surfaces, respectively, and a rigid rough surface with a power spectrum equal to the sum of the power spectra of the two original surfaces. It is assumed that surface contact comprises numerous spherical asperity microcontacts, which are sufficiently apart from each other in order for asperity interactions to be neglected as secondary. This is a reasonable assumption for the relatively small interference distances (or light contact loads) considered in this study. Based on these assumptions and knowledge of the mean contact pressure and real contact area at asperity microcontacts, the total contact load and real contact area can be obtained using an integration procedure. It is necessary, therefore, to derive a constitutive model for a single asperity microcontact.

In a previous study [26], the stress-strain behavior of asperities was assumed to be either purely elastic or fully plastic, i.e., the intermediate range of elastic-plastic deformation was not considered. Hertz theory can be used to analyze contact of elastically deformed asperities. For fully plastic microcontacts where the plastic zone is not contained by elastic material, the mean contact pressure is equal to the material hardness. However, as the interference distance at an asperity microcontact

increases, a gradual transition from elastic to fully plastic deformation occurs. In this regime, the plastic zone is small and fully contained by surrounding elastic material and the overall deformation behavior is elastic-plastic [5,6]. Therefore, to accurately determine the contact force between two approaching surfaces, the stress-strain constitutive relation and the real contact area corresponding to the elastic-plastic deformation regime should be incorporated into the previous elastic-fully plastic contact model [26].

A constitutive relation was obtained from a finite element model of a rigid sphere in normal contact with an elastic-perfectly plastic homogeneous half-space modeled by axisymmetric eight-node quadratic elements. The finite element mesh consisted of 5395 elements comprising 16622 nodes. The simulations were performed in 12 steps of 80 increments each. The typical computational time on an IBM RS6000 (580 model) workstation was about 18000 CPU seconds. The multi-purpose code ABAQUS was used to perform the finite element simulations. The mean contact pressure, p_m, and real contact area, a, were obtained in terms of the interference distance between the rigid sphere and the surface of the deformable medium, d. Figures 1 (a) and 1(b) show the normalized mean contact pressure, p_m / s_Y, and the truncated-to-real contact area ratio, a'/a, versus the representative strain, $E^* d / s_Y r'$, where s_Y is the yield strength of the deformable medium and r' is the radius of the truncated contact area a'. The representative strain is different from that used by Johnson [5] to describe the evolution of deformation in an elastic-perfectly plastic material indented by a sphere, defined as $E^* r / s_Y R$, where r is the radius of the real contact area and R is the radius of curvature of the rigid sphere. However, because the radius of the real contact area is not known from the geometric truncation, the interference and truncated radius were used to determine the representative strain.

Elastic, elastic-plastic, and fully plastic deformation regimes are distinguished in Fig. 1. Increasing the surface interference (or representative strain) yields a continuous increase of the mean contact pressure accompanied by a decrease of the contact area ratio. Figure 2 shows a comparison between results obtained with the present finite element model and the classical Hertz theory for an elastic half-space indented by a rigid sphere. The favorable comparison of the results of the two methods illustrates the suitability of the finite element model (for the present analysis involving only global variables, such as the contact pressure and contact area) and the correctness of the assumed boundary conditions.

The simulation results shown in Fig. 1 were used to derive relations for the mean contact pressure and contact area in terms of the local interference and elastic-plastic material properties. Thus, from curve fitting, the following constitutive relations were obtained.

For elastic deformation ($E^*\delta / \sigma_Y r' < 1.78$),

$$\frac{p_m}{\sigma_Y} = \frac{4\sqrt{2}}{3\pi}\left(\frac{E^*\delta}{\sigma_Y r'}\right), \qquad \frac{a'}{a} = 2\ . \tag{2}$$

For elastic-plastic deformation ($1.78 \le E^*\delta / \sigma_Y r' < 21$),

$$\frac{p_m}{\sigma_Y} = 0.70\ln\left(\frac{E^*\delta}{\sigma_Y r'}\right) + 0.66, \qquad \frac{a'}{a} = 0.05\left[\ln\left(\frac{E^*\delta}{\sigma_Y r'}\right)\right]^2 - 0.57\ln\left(\frac{E^*\delta}{\sigma_Y r'}\right) + 2.41. \tag{3}$$

For fully plastic deformation ($21 \le E^*\delta / \sigma_Y r' \le 400$),

$$\frac{p_m}{\sigma_Y} = 2.9, \qquad \frac{a'}{a} = 0.05\left[\ln\left(\frac{E^*\delta}{\sigma_Y r'}\right)\right]^2 - 0.57\ln\left(\frac{E^*\delta}{\sigma_Y r'}\right) + 2.41\ . \tag{4}$$

For fully plastic deformation ($400 < E^*\delta / \sigma_Y r'$),

$$\frac{p_m}{\sigma_Y} = 2.9, \qquad \frac{a'}{a} = 0.71 \tag{5}$$

Results for the mean contact pressure and contact radius obtained from Eqs. (2)-(5) were found to be in good agreement with finite elements results reported by Mesarovic and Fleck [6] for elastic-plastic homogeneous solids indented by a rigid sphere. In particular, the deformation regime defined by Eq. (5) is consistent with the plastic similarity regime reported in Ref. [6].

The constitutive relations given by Eqs. (2)-(5) are for a homogeneous elastic-plastic half-space. However, it is possible to extend the present contact model to layered media by appropriately modifying the above relations to include the effects of the mechanical properties of the layer and substrate materials and the layer thickness. This was accomplished by introducing the equivalent material properties in the constitutive relations given by Eqs. (2)-(5). Assuming that the yield strength is equal to one-third of the material hardness [29], the equivalent yield strength of a layered medium, $\sigma_{Y,e}$, can be expressed as [30]

$$\sigma_{Y,e} = \sigma_{Y,s} + \left(\sigma_{Y,l} - \sigma_{Y,s}\right)\exp\left[-\left(\frac{\delta}{t}\right)\left(\frac{E_s}{E_l}\right)^{1/2}\right], \tag{6}$$

where t is the overcoat thickness, E is the elastic modulus, and subscripts l and s denote the layer and substrate material properties, respectively. The equivalent effective elastic modulus of a layered medium, E_e^*, is given by [31]

$$E_e^* = \left[\left(1 - e^{-\alpha t/r\sqrt{p}}\right)\frac{1-\nu_l^2}{E_l} + e^{-\alpha t/r\sqrt{p}}\,\frac{1-\nu_s^2}{E_s} + \frac{1-\nu_i^2}{E_i}\right]^{-1}, \tag{7}$$

where α is a geometrical factor that depends on the indenter shape and can be determined numerically, ν is the Poisson's ratio, and subscript i denotes the indenter material. It is noted that only the elastic properties of the indenting surface are included in Eq. (7), i.e., plastic deformation is confined only in the

layered medium (Eq. (6)). Based on Eqs. (6) and (7), the nondimensional representative strain for a layered medium, $E_e^* \delta / \sigma_{Y,e} r'$, can be obtained as a function of the known mechanical properties of the indenter, layer, and substrate materials, layer thickness, and surface interference distance.

To validate the modified contact model, finite element simulation results for an elastic-plastic layered medium indented by a rigid sphere were contrasted with results obtained from the contact model (Eqs. (2)-(5)), using Eqs. (6) and (7) to account for the effects of the layer (overcoat) thickness and material properties. The finite element mesh, shown in Fig. 3, consists of 12063 axisymmetric eight-node isoparametric elements comprising 34337 nodes. The nodes of the left vertical boundary were fixed against displacement in the horizontal direction, whereas the nodes of the bottom boundary were fixed against displacement in the vertical direction. Simulations were performed for an overcoat thickness t = 2, 5, and 10 nm. The elastic modulus and yield strength of the overcoat material were set equal to 114 and 5.67 GPa and those of the substrate material equal to 130 and 2.67 GPa, respectively. To account for geometric nonlinearities resulting from large displacements, an updated Lagrangian formulation was adopted in the finite element analysis. The typical computational time for a simulation on a Pentium III 550 computer was approximately 40000 CPU seconds.

Figure 4 shows the normalized mean pressure as a function of the modified representative strain. The symbols represent finite element data corresponding to different overcoat thickness values. The solid curve is the solution obtained from the modified contact model (Eqs. (2)-(7)). The figure shows that the results are in excellent agreement. In addition to the mean contact pressure, it is also necessary to verify whether the prediction of the real contact area was accurate. Figure 5 shows a comparison between results for the normalized contact radius obtained from the modified contact model, r_{CM}/R (with

equivalent material properties given by Eqs. (6) and (7)) and the contact radius determined from the finite element analysis of the indented elastic-plastic layered medium, r_L/R, where R is the radius of the rigid sphere. The best-fit line to the data yields a correlation factor of 0.9992. The error between analytical and numerical results is less than 5%. In view of Figs. 4 and 5, it may be concluded that the contact constitutive model originally developed for homogenous media can be extended to layered media by introducing the equivalent material properties of the layered medium. The constitutive relations for the mean contact pressure and real contact area, reflecting a continuous transition from elastic to fully plastic deformation, were used in the three-dimensional contact analysis of rough surfaces characterized by fractal geometry described in the following section.

4. Surface Contact Model

As mentioned previously, the equivalent contact model of two rough surfaces comprises an elastic-plastic medium in contact with a rigid rough surface. The mechanical properties of the medium and the topography (described by fractal geometry) of the rough surface are equivalent to those of the contacting surfaces. As the rough surface approaches the deformable medium, asperity microcontacts are established over the simulated apparent contact area. Depending on the local surface interference and asperity radius, elastic, elastic-plastic, or fully plastic deformation may occur at asperity microcontacts. Following an analytical procedure similar to that detailed elsewhere [26], the total contact load and real contact area at a given maximum surface interference distance, $d_{\max}$, was calculated from the total truncated contact area of the rough surface, S', given by,

$$S' = \int_{a'_S}^{a'_L} a' n(a') da', \tag{8}$$

where a' is the truncated area of a microcontact, a'_L and a'_S are the largest and smallest truncated microcontact areas, respectively, and $n(a')$ is the truncated asperity size distribution function. At a given surface interference, the number of microcontacts with truncated areas between a' and $a'+da'$ is given by $n(a')da'$. For a continuum description, the size of the smallest microcontact should be greater than the atomic dimensions; thus, the diameter of the smallest truncated area, a'_S, is assumed to be equal to six times the lattice dimension of the overcoat material.

The number of truncated asperities, *N*, with areas greater than a particular truncated area, a', is assumed to follow the power-law relation [15],

$$N(a') = \left(\frac{a'_L}{a'} \right)^{(D-1)/2} . \tag{9}$$

Consequently, the truncated asperity size distribution function can be expressed as [26]

$$n(a') = -\frac{dN(a')}{da'} = \frac{(D-1)}{2a'_L} \left(\frac{a'_L}{a'} \right)^{(D+1)/2} . \tag{10}$$

Substituting Eq. (10) into Eq. (8), the total truncated area of the fractal surface can be written as

$$S' = \frac{D-1}{3-D} \left(a'_L - a'_L{}^{(D-1)/2} \; a'_S{}^{(3-D)/2} \right). \tag{11}$$

At a given surface interference, the total truncated contact area, S', can be obtained by numerical integration. Using a grid mesh of size equal to the diameter of the smallest truncated microcontact, a'_s, the number of surface points above the truncation plane was determined and the total truncated area was obtained as the apparent area multiplied by the ratio of the number of truncated surface points to the total number of grid points. From the obtained total truncated area, S', the

truncated area of the largest microcontact, a'_L, was calculated from Eq. (11). Hence, a series of truncated asperities can be generated using Eq. (9). Figure 6 shows a comparison between analytical results (obtained from Eq. (11) for $a'_s = 0$) and numerical results for small surface interference distances, typical of those used in the surface contact simulations. The fair agreement between the results of the two methods suggests that the assumption of a power-law asperity distribution is reasonable.

The local interference, δ_i, at the ith asperity is given by [26]

$$\delta_i = 2G^{(D-2)}(\ln \gamma)^{1/2}(2r_i')^{(3-D)}. \tag{12}$$

As discussed in the previous section, the representative strain at an asperity microcontact, $E^*\delta_i / \sigma_Y r_i'$, in the case of a layered medium can be obtained in terms of the equivalent yield strength and equivalent (effective) elastic modulus given by Eqs. (6) and (7), respectively. However, because the equivalent elastic modulus is a function of the real contact radius, which is not known *a priori*, an iteration procedure was used to determine the equivalent elastic modulus and real contact radius from Eqs. (2)-(5) and (7). The initial value of the real contact radius was assumed to be equal to the truncated radius. Using this iteration scheme for the calculation of the equivalent elastic modulus, the representative strain was found and a new value was obtained for the real contact radius. This iteration procedure was repeated until the change in the real contact radius approached a specified small tolerance value (e.g., 1%). Typically, six or seven iterations were required to obtain the equivalent elastic modulus and real contact radius. Subsequently, the mean contact pressure, $p_{m,i}$, and real contact area, a_i, at the ith asperity microcontact were determined from the appropriate constitutive relations

(Eqs. (2)-(5)), depending on the deformation regime. The contact force at the ith asperity, dL_i, is given by

$$dL_i = p_{m,i} a_i . \tag{13}$$

The total contact force, L, and total real contact area, A_r, were obtained by numerical integration,

$$L = \sum_{i=1}^{N(a'_s)} dL_i = \sum_{i=1}^{N(a'_s)} p_{m,i} a_i , \tag{14}$$

and

$$A_r = \sum_{i=1}^{N(a'_s)} a_i , \tag{15}$$

where $N(a'_s)$ is the total number of truncated asperities. The advantage of this analytical method is that it requires significantly less computational time than other numerical techniques requiring a large and very fine mesh, such as the finite element method.

5. Results and Discussion

Figure 7 shows a 1 μm x 1 μm fractal surface generated from Eq. (1) for D = 2.44, G = 9.46 × 10^{-13} m, M = 10, g = 1.5, L = 1 μm, and L_s equal to six times the lattice dimension of carbon. Since the sample length, L, was chosen to be smaller than the upper limit of the sample length for fractal characterization [24,32], the entire apparent contact area (Fig. 7) can be described by fractal geometry. The fractal parameters D and G were determined from a log-log plot of the structure function versus wavelength of a surface profile equivalent to those of a magnetic head and a smooth (rms ~0.2 nm) thin-film disk imaged with an atomic force microscope [32]. The power spectrum of the equivalent surface,

shown in Fig. 8, is equal to the sum of the power spectra of the head and the disk surfaces. Isotropic random surfaces are characterized by axially symmetric power spectra. With the exception of two orthogonal bands along the frequency axes, the power spectrum in Fig. 8 shows axial symmetry. As explained in a previous study [26], these artificial bands occur due to the unmatchness of the opposing boundaries of the simulated surface and can be removed using the simple technique proposed by Anguiano et al. [33].

Contact simulations were performed for a hard disk coated with a carbon overcoat possessing an elastic modulus of 114 GPa and yield strength of 5.67 GPa in contact with a tri-pad picoslider coated with a carbon overcoat (Fig. 9). In view of the small surface interference distances examined, the elastic modulus of the picoslider surface was set equal to that of the carbon overcoat for simplicity. Contact was assumed to occur only at the trailing edge of the center-pad of the picoslider, which has an apparent contact area of 250 $\mu m \times$ 40 μm. The contact loads and corresponding real contact areas determined from simulations performed on 1 μm x 1 μm surface areas (such as that shown in Fig. 7) were multiplied by a factor of 10^4 in order to convert them to picoslider data. These are obviously upper bound results since the picoslider may contact the disk surface at some angle, i.e., the actual apparent contact area may be a portion of the trailing edge of the picoslider's center-pad.

For the range of surface interferences considered in this study, the multi-layered disk medium can be simplified to a two-layered medium. This is because the stress and strain fields are confined within the carbon overcoat and the magnetic layer [32]. To reveal the effects of the surface topography and overcoat thickness on the magnitude of the contact load and deformation behavior, results for the contact load and real contact area are presented for a homogeneous medium with carbon overcoat properties and different fractal parameters, followed by results for a layered medium with a carbon

overcoat of varying thickness and surface topography identical to that of the homogeneous medium.

Figures 10(a) and 10(b) show the variation of the total contact load on the picoslider, L, and the real to apparent contact area ratio, A_r/A_a, with the maximum surface interference distance, d_{max}. The elastic and plastic (including both elastic-plastic and fully plastic microcontacts) components of each parameter are also plotted in order to elucidate the dominant deformation mode as a function of the maximum interference distance. Both the elastic and the plastic components of the contact load and the real contact area increase rapidly with increasing surface interference at the head-disk interface. However, the contribution of the plastic component is secondary, except at very small surface interferences. This is expected because at small surface interferences (or low contact loads) actual contact occurs at the smaller (sharper) asperities residing on top of larger asperities. Because it is easier for the yield condition to be satisfied at the smaller microcontacts [26], the resulting deformation behavior at small surface interferences is predominantly inelastic (i.e., elastic-plastic and fully plastic). Figure 10(b) shows that the real contact area is a very small fraction of the apparent contact area. Since the typical load on a picoslider (in the absence of high adhesion forces) is below 1 g, the corresponding real contact area is significantly less than 1% of the apparent contact area.

The significance of the fractal dimension D and fractal roughness G on the contact load and real contact area can be interpreted in light of the results shown in Figs. 11 and 12, respectively. For fixed fractal roughness and maximum surface interference, increasing the fractal dimension increases the contact load and the real contact area significantly (Fig. 11). This is expected because larger D values are associated with smoother (denser) surface profiles, which, obviously, exhibit a greater load bearing capacity due to the resulting larger real contact areas. A similar trend occurs when the fractal roughness G decreases and the fractal dimension D is fixed (Fig. 12). Since G is a height scaling parameter, higher

G values correspond to rougher (less dense) surface topographies characterized by a lower load bearing capacity due to the smaller real contact areas produced. Roughening (texturing) for reducing intimate surface contact is a well-established technique used in various tribological systems to suppress the occurrence of high adhesion forces (stiction), such as in disk drives and microelectromechanical systems. A comparison of Figs. 11(c) and 12(c) shows that the effect of the fractal roughness G on the portion of the real contact area undergoing inelastic deformation, $A_{r,p}$, is relatively less pronounced than that of the fractal dimension D. It appears that the evolution of plasticity at the contact region reaches a maximum for a fractal roughness value of the order of $\sim 10^{-13}$ m (Fig. 12(c)).

To illustrate the effect of the substrate material (magnetic layer) on the magnitudes of the contact load and real contact area, results for a homogeneous half-space with carbon overcoat material properties and a layered medium with a carbon overcoat of thickness t = 2, 5, and 10 nm are contrasted in Figs. 13 and 14. The surface topography was generated from Eq. (1) using the parameters of the surface shown in Fig. 7. As expected, the effect of the underlying magnetic medium is insignificant at small surface interference distances (or light contact loads). In all cases, increasing the surface interference produces a pronounced increase in the contact load (Fig. 13(a)) and the inelastic portion of the real contact area (Fig. 13(b)). However, as the overcoat thickness increases from 2 to 10 nm the results for the layered medium gradually approach those of the homogeneous medium. This is because a stronger substrate effect is encountered with thinner overcoats and the elastic modulus of the magnetic medium (i.e., the substrate of the layered medium) is greater than that of the carbon overcoat. Since the deformation at the contact region is predominantly elastic, illustrated by the extremely small fraction of inelastically deformed asperity microcontacts (Fig. 13(b)) and by comparing the elastic and plastic contact load components, L_e and L_p, shown in Figs. 14(a) and 14(b), respectively, higher contact loads

are obtained with the stiffer layered medium. Thus, a slightly higher contact load is produced with the 2-nm-thick overcoat due to the most pronounced effect of the stiffer substrate. Figure 14 indicates that the main difference in the contact load results for layered and homogeneous media is due to the dominance of elastic deformation, whereas differences between the results for overcoats of different thickness are attributed to the effect of the substrate material (magnetic medium), which depends on the overcoat thickness.

6. Conclusions

A three-dimensional contact model was developed for elastic-plastic layered media with rough surfaces characterized by fractal geometry. Numerical results were presented for the head-disk contact interface using realistic surface topographies, constructed from a truncated W-M function with fractal parameters obtained from a surface equivalent to those of a magnetic recording head and a smooth carbon-coated thin-film disk. Based on the obtained results and discussions, the following main conclusions can be drawn.

(1) Constitutive relations for the mean contact pressure and real contact area versus a representative strain parameter were derived from a finite element model of a rigid sphere indenting an elastic-plastic medium. The constitutive model accounts for elastic, elastic-plastic, and fully plastic deformation at asperity microcontacts.

(2) The representative strain in the constitutive model is a local deformation parameter that depends on the mechanical properties of the contacting surfaces, the local surface interference distance, and the contact radius of the truncated asperities.

(3) For a given surface topography of the head-disk interface, both the contact load and the real

contact area at the trailing edge of the center-pad of a picoslider increase monotonically with increasing maximum surface interference distance.

(4) The contact load decreases with decreasing fractal dimension D and/or increasing fractal roughness G. This is due to the effect of fractal parameters on the load bearing surface area. The effect of the mechanical properties of the magnetic medium on the contact load and deformation behavior at the real contact area becomes more pronounced with decreasing overcoat thickness.

(5) For the surface interference range examined, the effect of the overcoat thickness on the contact load and real contact area is relatively small and the dominant deformation mode at asperity microcontacts is elastic.

ACKNOWLEDGEMENTS

This research was partially supported by the Surface Engineering and Tribology Program of the National Science Foundation under Grant No. CMS-9734907, National Storage Industry Consortium (NSIC), Extremely High Density Recording (EHDR) Program, and Computer Mechanics Laboratory at the University of California at Berkeley. The authors are grateful to H. Zhu for the information provided about the slider dimensions.

REFERENCES

[1] Aleksandrov, V. M., Babeshko, V. A., and Kucherov, 1966, "Contact Problems for an Elastic Layer of Slight Thickness," *Journal of Applied Mathematics and Mechanics*, **39**, pp. 124-142.

[2] Aldlas, J. B., and Kuipers, M., 1970, "On the Two Dimensional Problem of a Cylindrical Stamp

Pressed into a Thin Elastic Layer," *Acta Mechanica*, **9**, pp. 292-311.

[3] Pao, Y. C., Wu, T.-S., and Chiu, Y. P., 1971, "Bounds on the Maximum Contact Stress of an Indented Elastic Layer," *ASME Journal of Applied Mechanics*, **38**, pp. 608-614.

[4] Ling, F. F., and Lai, W. M., 1980, "Surface Mechanics of Layered Media," *Solid Contact and Lubrication*, Cheng, H. S., and Keer, L. M., eds., AMD-Vol. 39, ASME, New York, pp. 27-50.

[5] Johnson, K. L., 1985, *Contact Mechanics*, Cambridge University Press, Cambridge, UK.

[6] Mesarovic, S. Dj., and Fleck, N. A., 1999, "Spherical Indentation of Elastic-Plastic Solids," *Proceedings of the Royal Society* (London), Series A, **455**, pp. 2707-2728.

[7] Kennedy, F. E., and Ling, F. F., 1974, "Elasto-Plastic Indentation of a Layered Medium," ASME *Journal of Engineering Materials and Technology*, **96**, pp. 97-103.

[8] Van der Zwaag, S., and Field, J. E., 1982, "The Effect of Thin hard Coatings on the Hertzian Stress Field," *Philosophical Magazine A*, **46**, pp. 133-150.

[9] Komvopoulos, K., 1988, "Finite Element Analysis of a Layered Elastic Solid in Normal Contact With a Rigid Surface," ASME *Journal of Tribology*, **110**, pp. 477-485.

[10] Komvopoulos, K., 1989, "Elastic-Plastic Finite Element Analysis of Indented Layered Media," ASME *Journal of Tribology*, **111**, pp. 430-439.

[11] Tian, H., and Saka, N., 1991, "Finite Element Analysis of an Elastic-Plastic Two-Layer Half-Space: Normal Contact," *Wear*, **148**, pp. 47-68.

[12] Kral, E. R., and Komvopoulos, K., 1996, "Three-Dimensional Finite Element Analysis of Surface Deformation and Stresses in an Elastic-Plastic Layered Medium Subjected to Indentation and Sliding Contact Loading," ASME *Journal of Applied Mechanics*, **63**, pp. 365-375.

[13] Greenwood, J. A., and Williamson, J. B. P., 1966, "Contact of Nominally Flat Surfaces," *Proceedings of the Royal Society* (London), Series A, **295**, pp. 300-319**.**

[14] Larsson, J., Biwa, S., and Storåkers, 1999, "Inelastic Flattening of rough Surfaces," *Mechanics of Materials*, **31**, pp. 29041.

[15] Mandelbrot, B. B., 1983, *The Fractal Geometry of Nature*, Freeman, New York.

[16] Borodich, F. M., and Onishchenko, D. A., 1999, "Similarity and Fractality in the Modeling of Roughness by a Multilevel Profile with Hierarchical Structure," *International Journal of Solids and Structures*, **36**, pp. 2585-2612.

[17] Majumdar, A., and Tien, C. L., 1990, "Fractal Charactaerization and Simulation of rough Surfaces," *Wear*, **136**, pp. 313-327.

[18] Berry, M. V., and Lewis, Z. V., 1980, "On the Weierstrass-Mandelbrot Fractal Function," *Proceedings of Royal Society (London)*, Series A, **370**, pp. 459-484.

[19] Majumdar, A., and Bhushan, B., 1991, "Fractal Model of Elastic-Plastic Contact Between Rough Surfaces," ASME *Journal of Tribology*, **113**, pp. 1-11.

[20] Blackmore, D., and Zhou J. G., 1998, "Fractal Analysis of Height Distributions of Anisotropic Rough Surfaces," *Fractals*, **6**, pp. 43-58.

[21] Blackmore, D., and Zhou G., 1998, "A New Fractal Model for Anisotropic Surfaces," *Int. J. Mach. Tools Manufact*., **38**, pp. 551-557.

[22] Ciavarella, M., Demelio, G., Barber, J. R., and Jang, Y. H., 2000, "Linear Elastic Contact of the Weierstrass Profile," *Proceedings of the Royal Society* (London), Series A, **456**, pp. 387-405.

[23] Wang, S. and Komvopoulos, K., 1994, "A Fractal Theory of the Interfacial Temperature Distribution in the Slow Sliding Regime: Part I — Elastic Contact and Heat Transfer Analysis," ASME *Journal of Tribology*, **116**, pp. 812-823.

[24] Wang, S. and Komvopoulos, K., 1994, "A Fractal Theory of the Interfacial Temperature Distribution in the Slow Sliding Regime: Part II — Multiple Domains, Elastoplastic Contacts and Applications," ASME *Journal of Tribology*, **116**, pp. 824-832.

[25] Wang, S. and Komvopoulos, K., 1995, "A Fractal Theory of the Temperature Distribution at Elastic Contacts of Fast Sliding Surfaces," ASME *Journal of Tribology*, **116**, pp. 824-832.

[26] Yan, W., and Komvopoulos, K., 1998, "Contact Analysis of Elastic-Plastic Fractal Surfaces," *Journal of Applied Physics*, **84**, pp. 3617-3624.

[27] Ausloos, M., and Berman, D. H., 1985, "A Multivariable Weierstrass-Mandelbrot Function," *Proceedings of the Royal Society (London)*, Series A, **400**, pp. 331-350.

[28] Russ, J. C., *Fractal Surfaces*, Plenum Press, New York, 1994, p. 168.

[29] Tabor, D., 1970, "The Hardness of Solids," *Review of Physics in Technology*, **1**, pp. 145-179.

[30] Bhattacharya, A. K., and Nix, W. D., 1988, "Analysis of Elastic and Plastic Deformation Associated with Indentation Testing of Thin Films on Substrates," *International Journal of Solids and Structures*, **24**, pp. 1287-1298.

[31] King, R. B., 1987, "Elastic Analysis of Some Punch Problems for a Layered Medium," *International Journal of Solids and Structures*, **23**, pp.1657-1664.

[32] Komvopoulos, K., 2000, "Head-Disk Interface Contact Mechanics for Ultrahigh Density Magnetic Recording," *Wear*, **238**, pp. 1-11.

[33] Anguiano, E., Pancorbo, M., and Aguilar, M., 1994, *Fractals in the Natural and Applied Sciences*, Novak, M. M., ed., Elsevier Science, New York, pp. 37-46.

List of Figures

surface interference distance for a homogeneous medium with carbon overcoat material properties ($G = 9.46 \times 10^{-13}$ m, $M = 10$, $g = 1.5$, and $L = 1$ μm).

Fig. 12 Effect of fractal roughness G on (a) contact load, (b) ratio of real to apparent contact area, and (c) ratio of inelastic portion of real contact area to apparent contact area versus maximum surface interference distance for a homogeneous medium with carbon overcoat material properties ($D = 2.44$, $M = 10$, $g = 1.5$, and $L = 1$ μm).

Fig. 13 (a) Contact load and (b) ratio of inelastic portion of real contact area to apparent contact area versus maximum surface interference for a homogeneous medium with carbon overcoat material properties and a layered medium consisting of a carbon overcoat with thickness 2, 5, and 10 nm and a substrate with magnetic medium material properties ($D = 2.44$, $G = 9.46 \times 10^{-13}$ m, $M = 10$, $g = 1.5$, and $L = 1$ μm).

Fig. 14 (a) Elastic and (b) plastic (including both elastic-plastic and fully plastic) contact load components versus maximum surface interference for a homogeneous medium with carbon overcoat material properties and a layered medium consisting of a carbon overcoat with thickness 2, 5, and 10 nm and a substrate with magnetic medium material properties ($D = 2.44$, $G = 9.46 \times 10^{-13}$ m, $M = 10$, $g = 1.5$, and $L = 1$ μm).

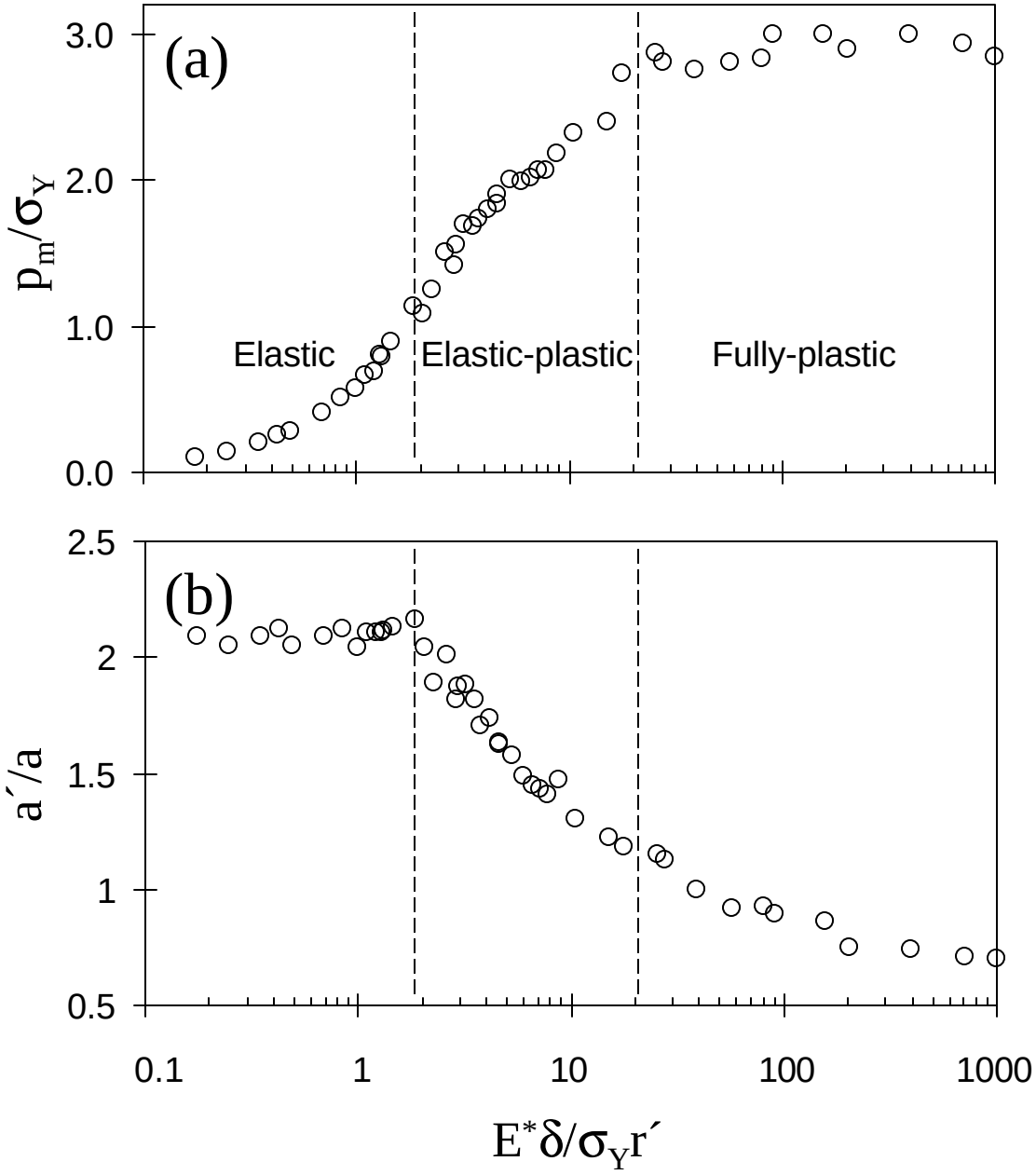
(a)
3.0
2.0
1.0
0.0
p_m/σ_Y
Elastic
Elastic-plastic
Fully-plastic
(b)
2.5
2
1.5
1
0.5
a´/a
0.1
1
10
100
1000
$E^*\delta/\sigma_Y r´$

Figure 1

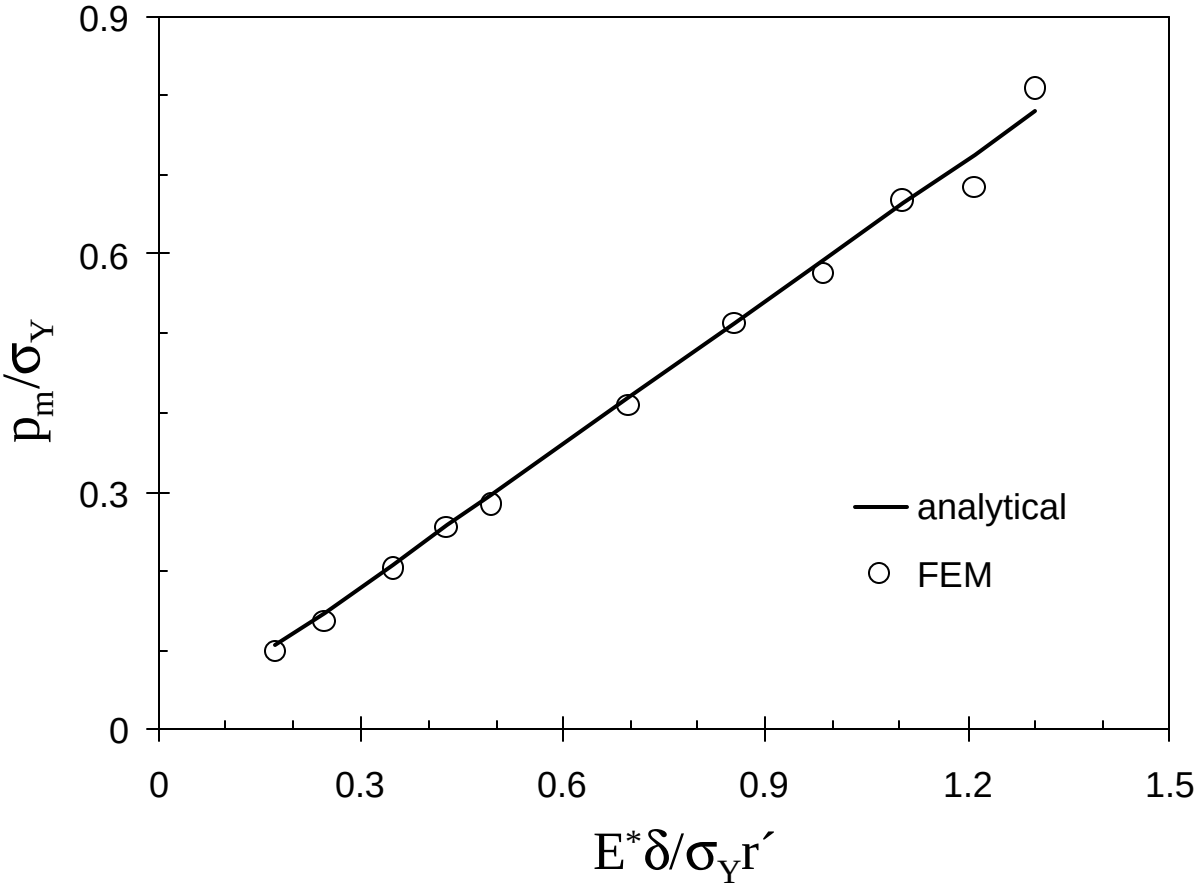
0.9
0.6
0.3
0
0
0.3
0.6
0.9
1.2
1.5
p_m/σ_Y
$E^*\delta/\sigma_Y r'$
analytical
FEM

Figure 2

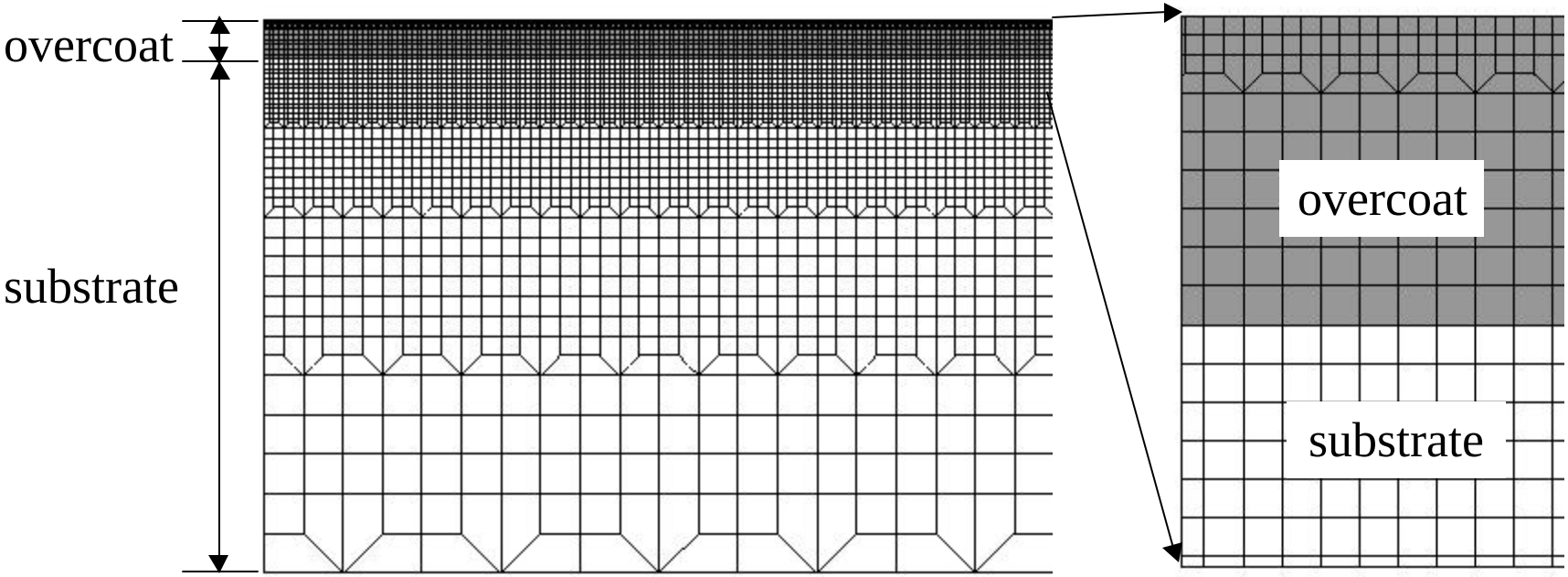

Figure 3

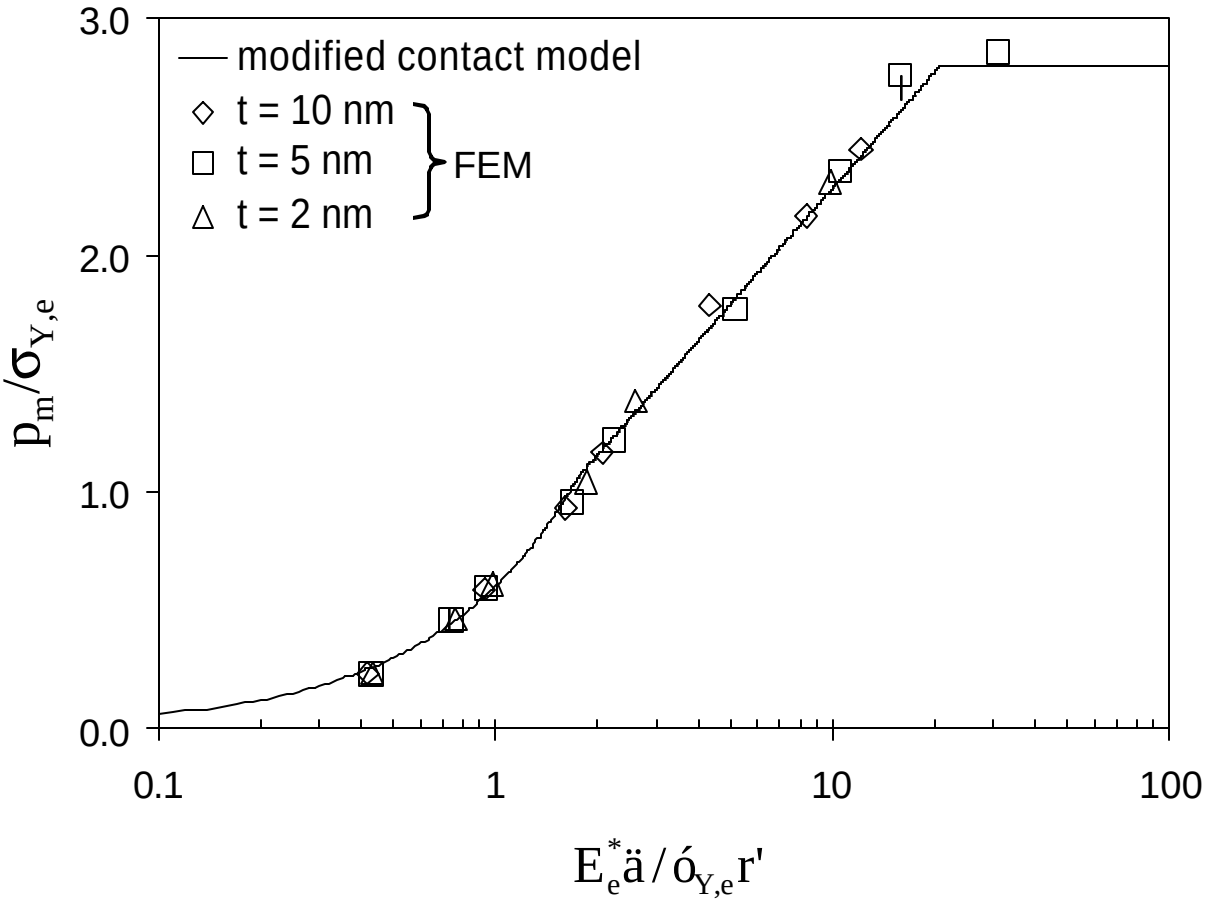
3.0
2.0
1.0
0.0
0.1
1
10
100
modified contact model
t = 10 nm
t = 5 nm
t = 2 nm
FEM
$p_m/\sigma_{Y,e}$
$E_e^* \ddot{a} / \acute{o}_{Y,e} r'$

Figure 4

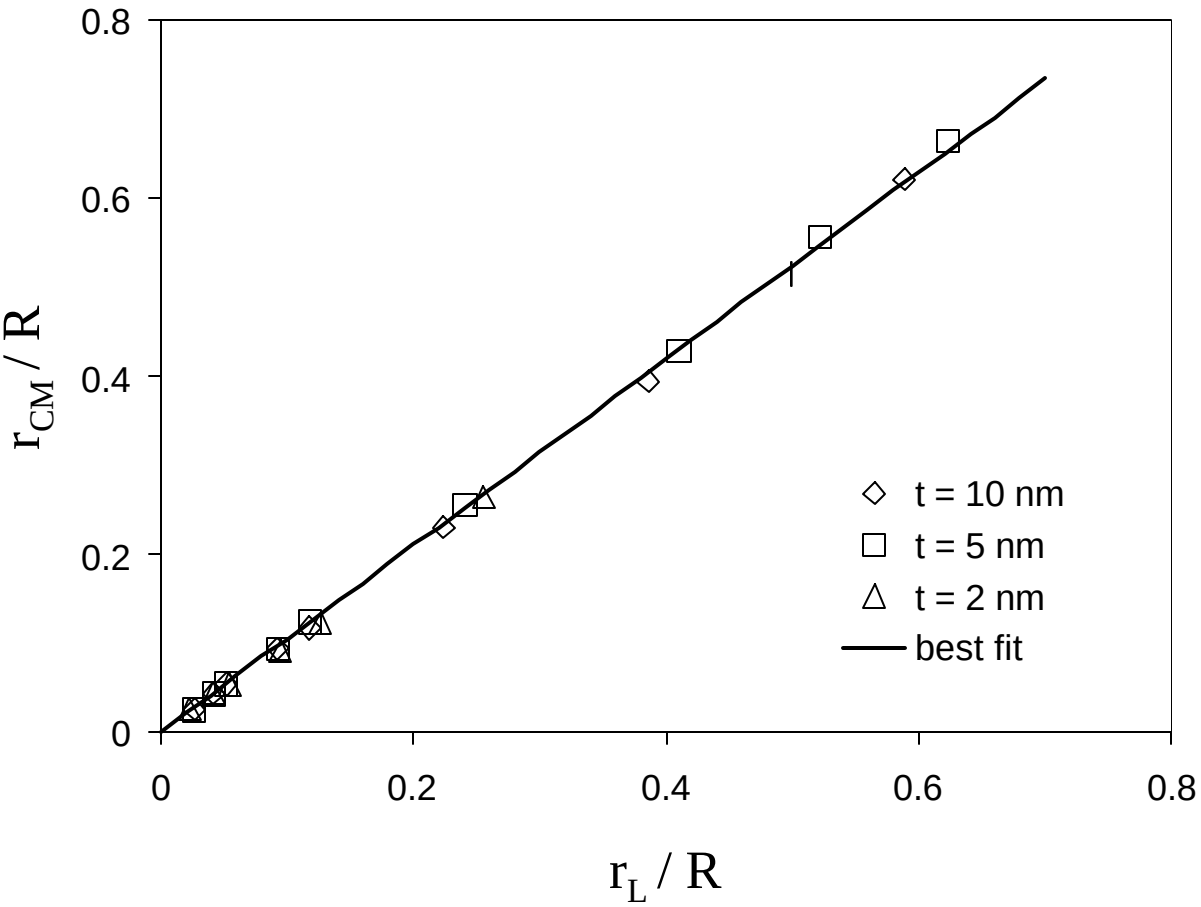

Figure 5

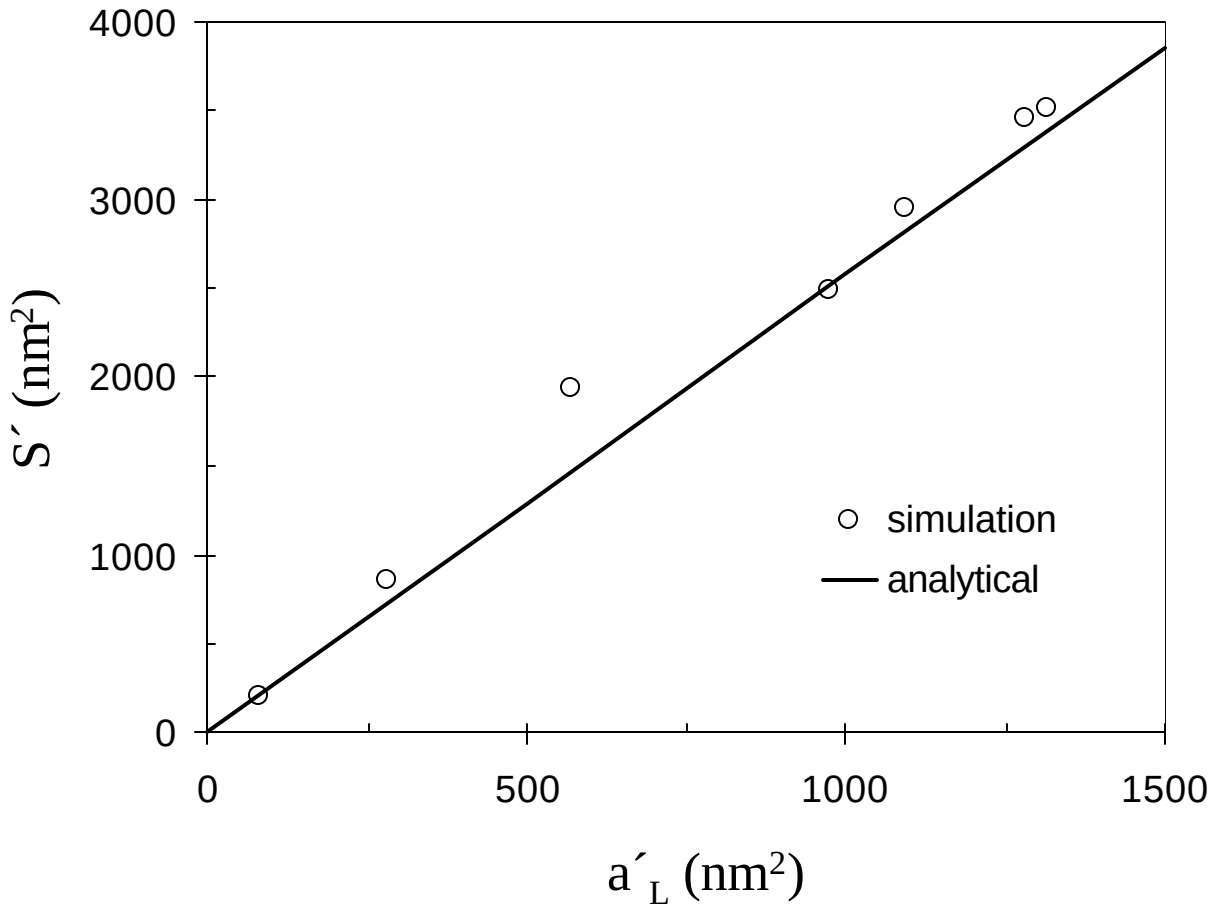
4000
3000
2000
1000
0
S´ (nm²)
0
500
1000
1500
a´L (nm²)
simulation
analytical

Figure 6

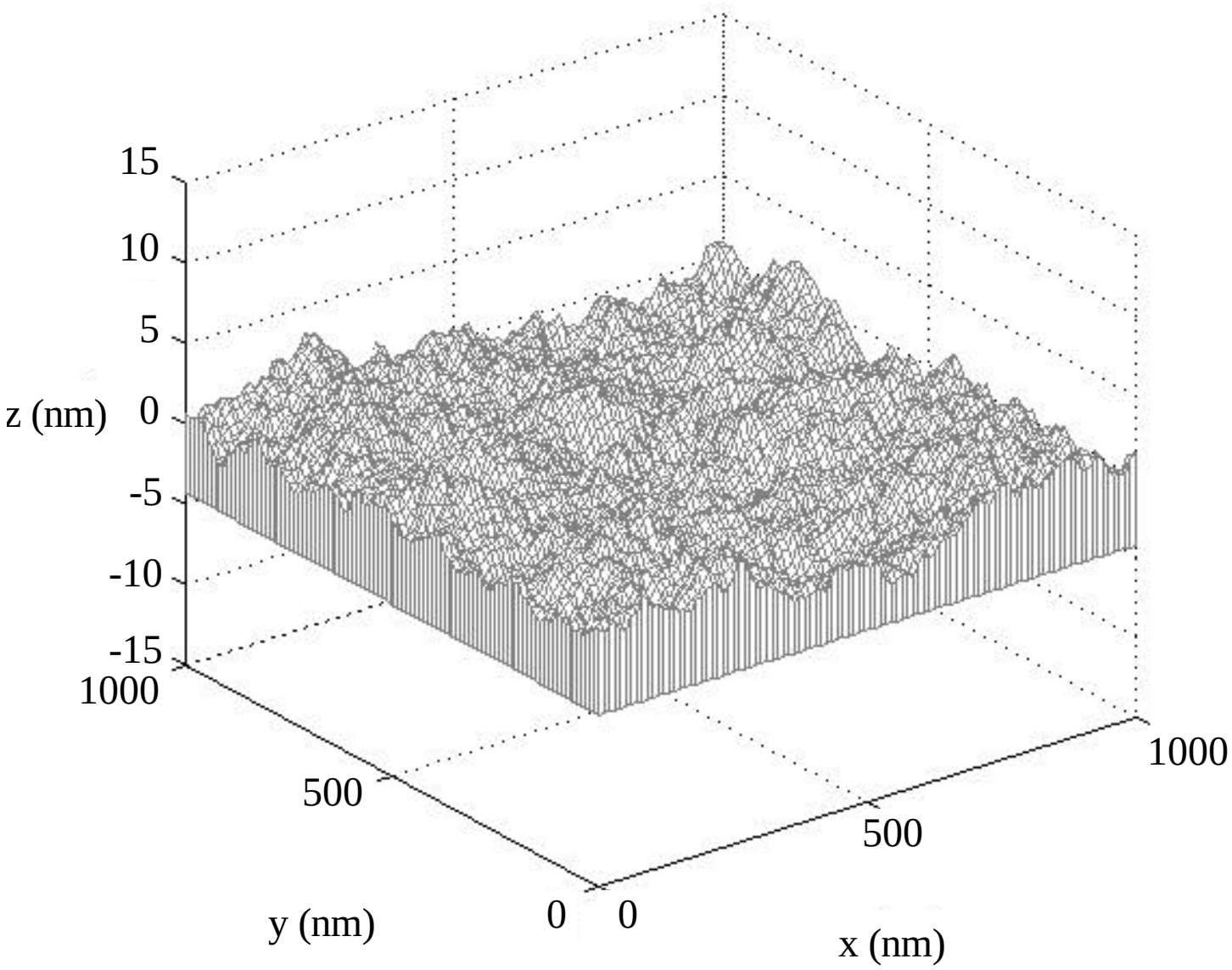

Figure 7

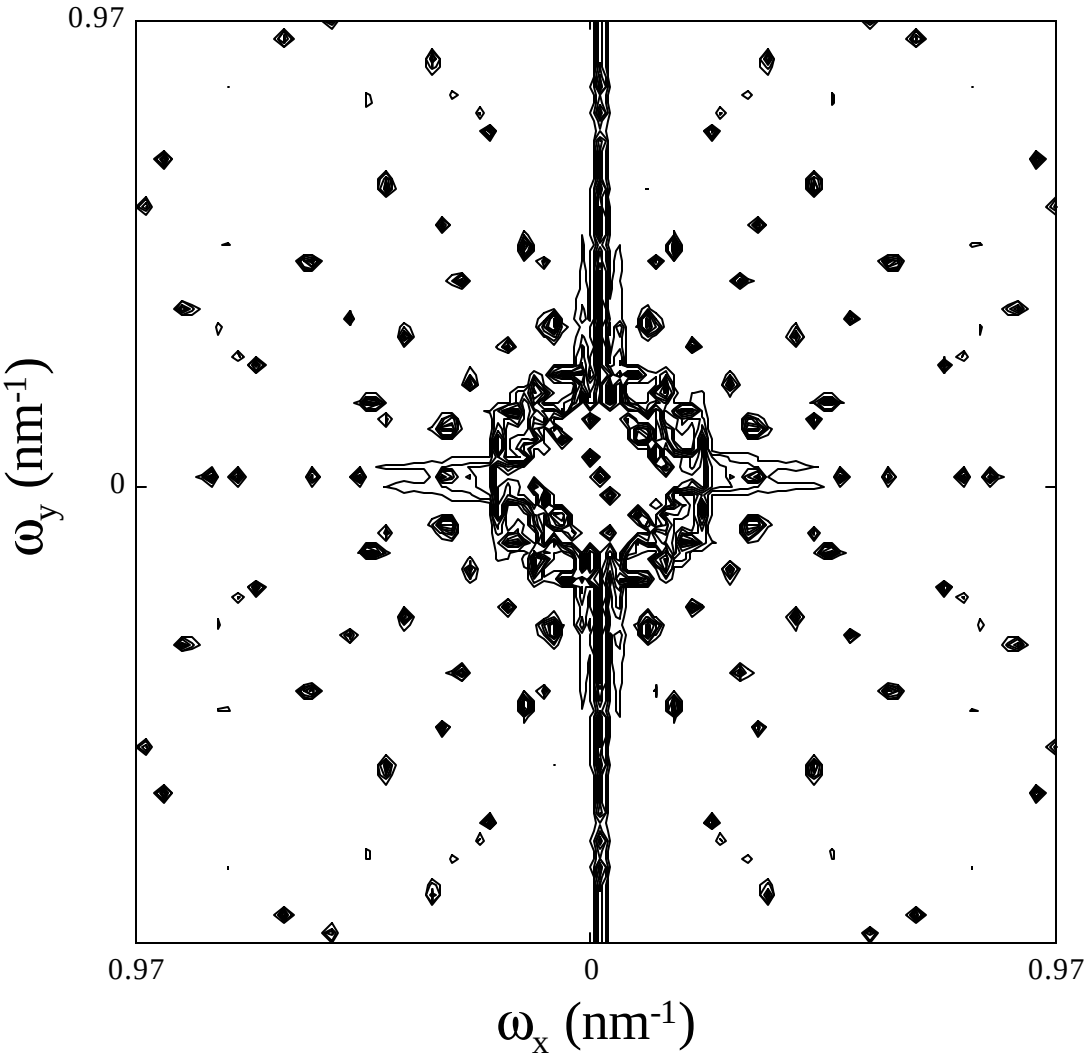

Figure 8

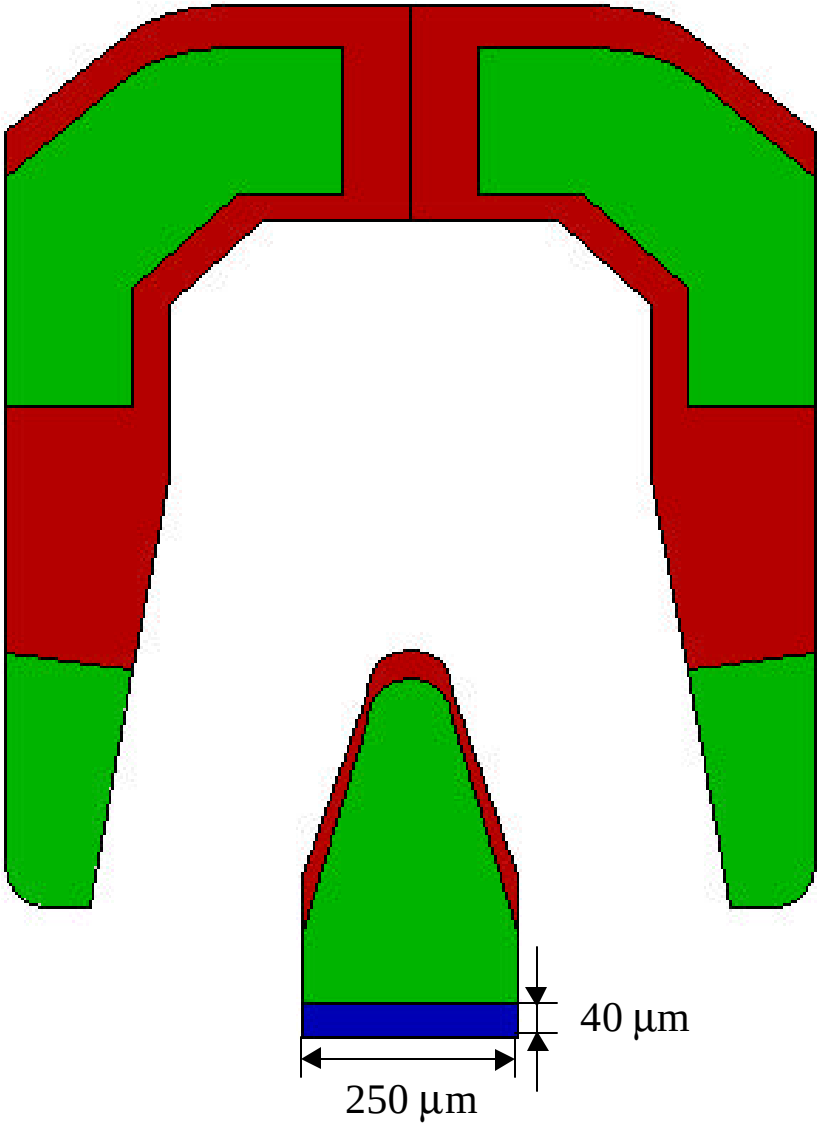

Figure 9

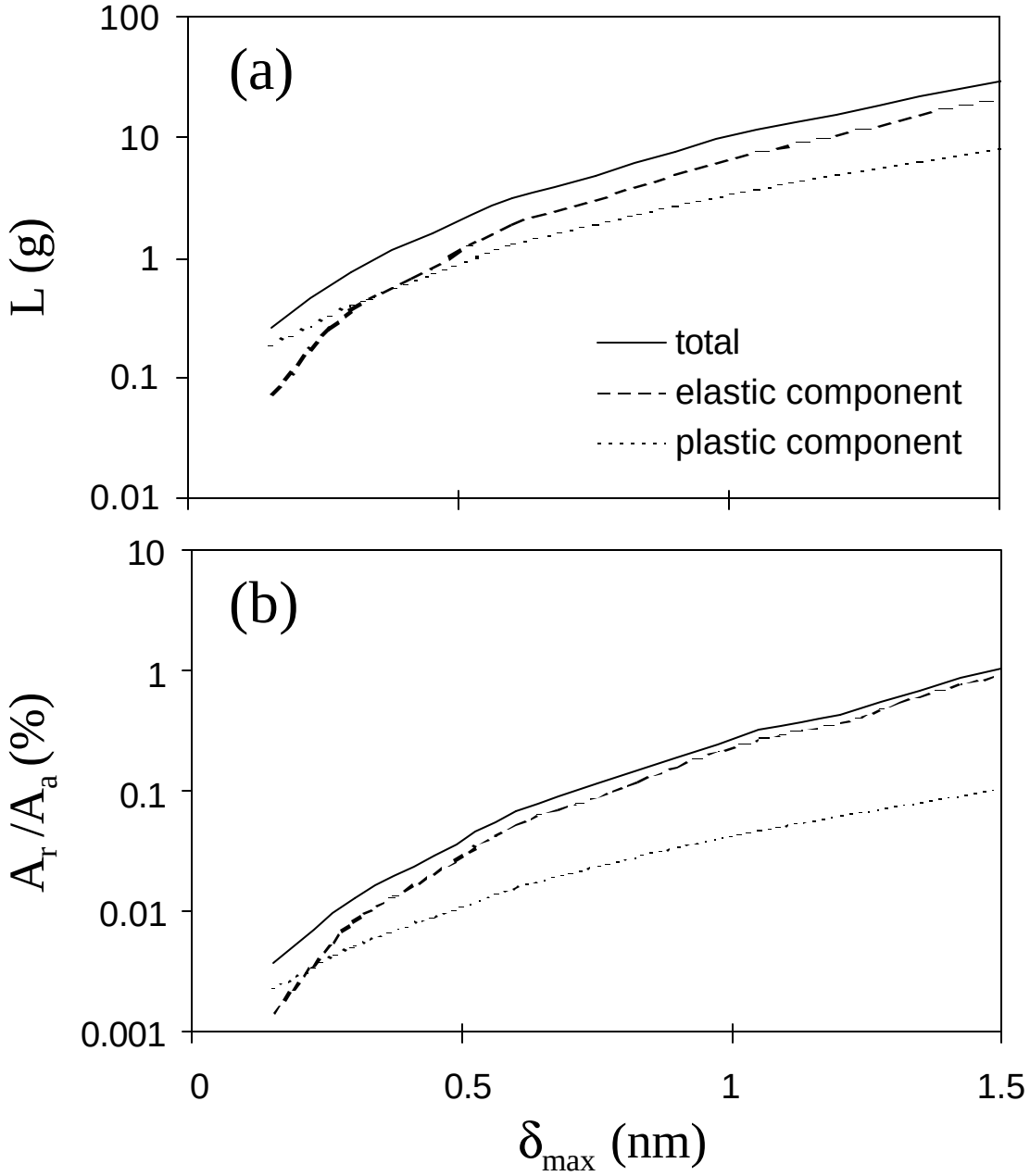
(a)
100
10
1
0.1
0.01
L (g)
total
elastic component
plastic component
(b)
10
1
0.1
0.01
0.001
A_r/A_a (%)
0
0.5
1
1.5
δ_{max} (nm)

Figure 10

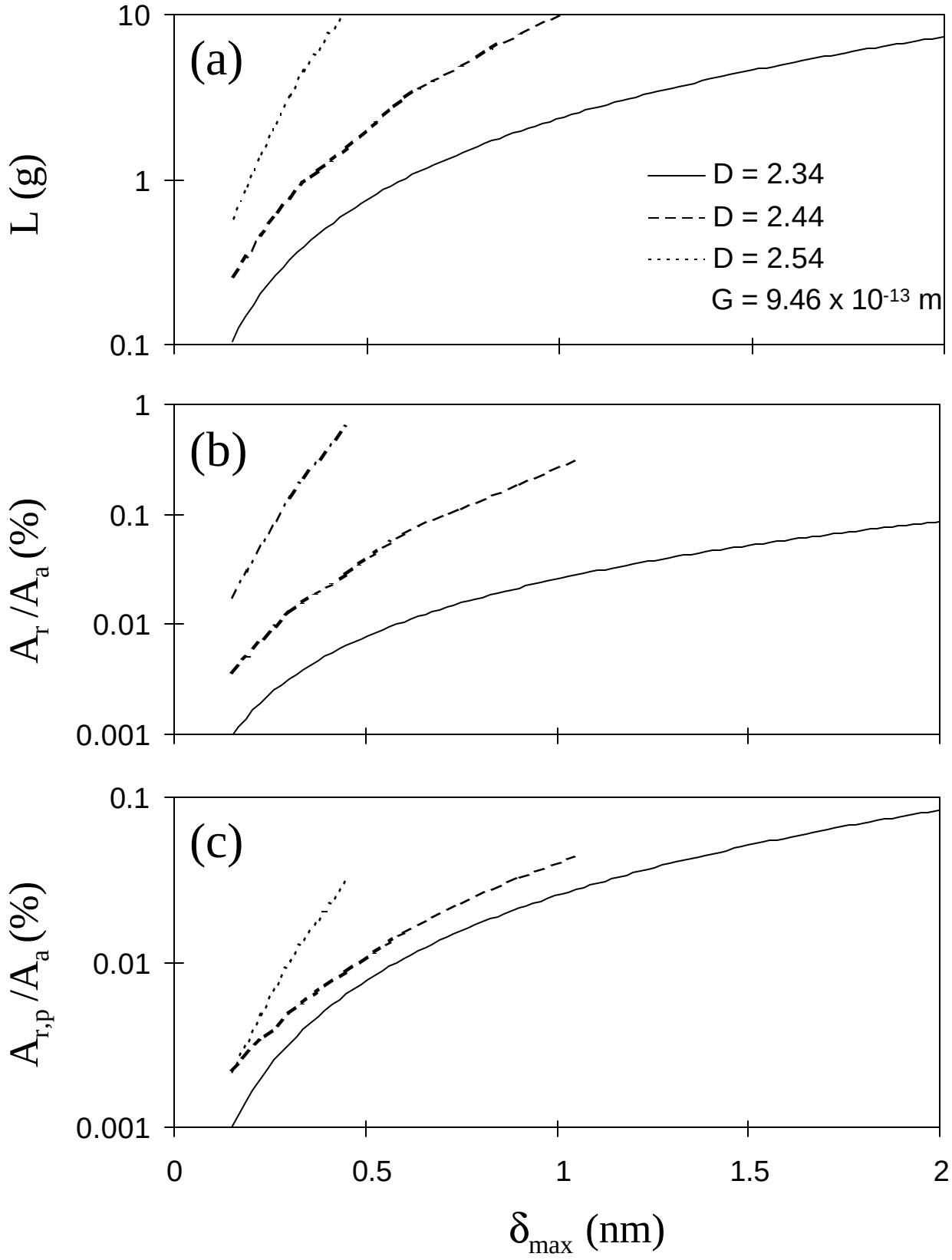
(a)
(b)
(c)
L (g)
A_r/A_a (%)
$A_{r,p}/A_a$ (%)
10
1
0.1
0.01
0.001
0
0.5
1
1.5
2
δ_{max} (nm)
D = 2.34
D = 2.44
D = 2.54
G = 9.46 x 10^{-13} m

Figure 11

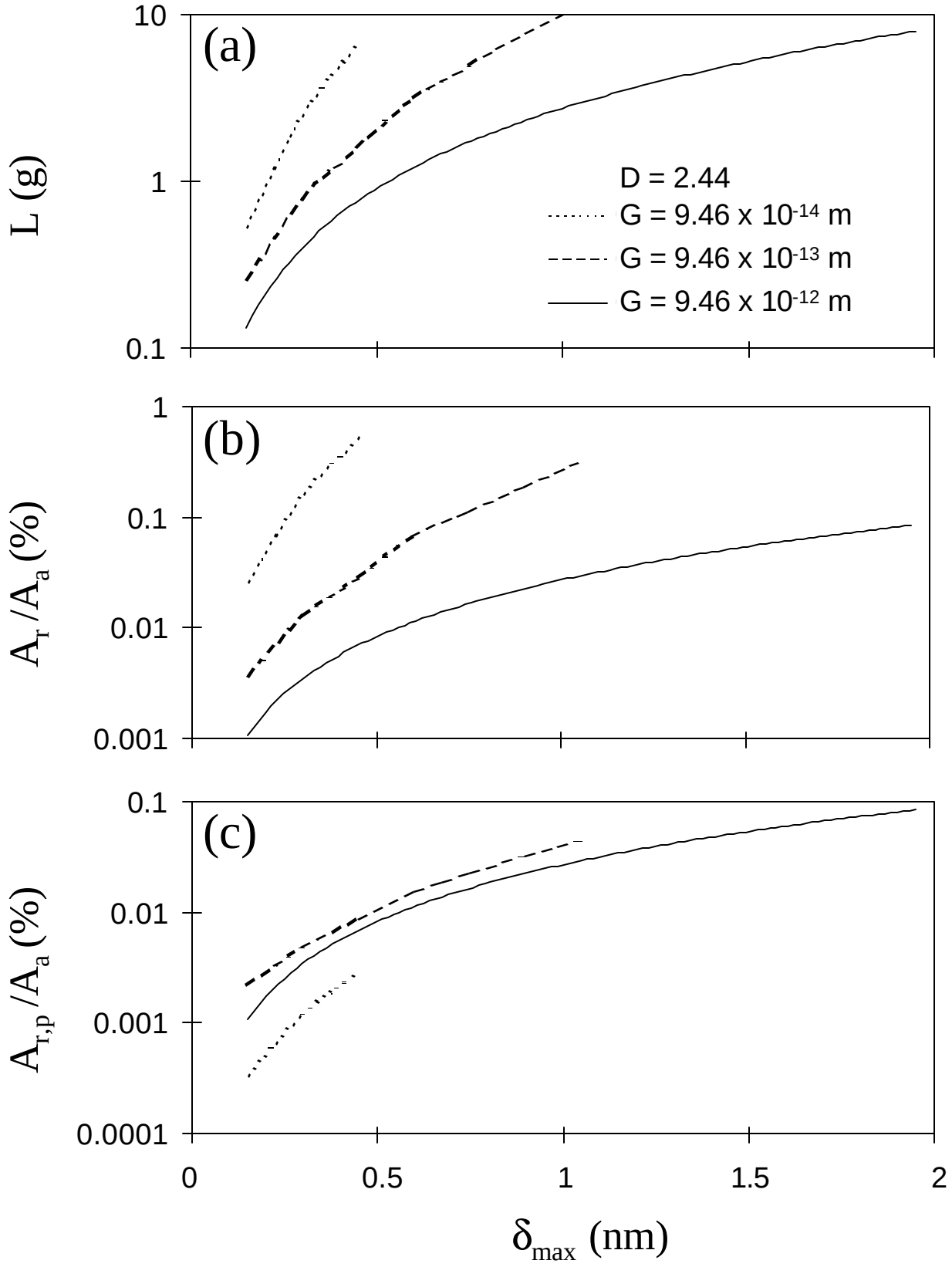
(a)
(b)
(c)
L (g)
A_r/A_a (%)
$A_{r,p}/A_a$ (%)
δ_{max} (nm)
D = 2.44
G = 9.46 x 10-14 m
G = 9.46 x 10-13 m
G = 9.46 x 10-12 m
10
1
0.1
0.01
0.001
0.0001
0
0.5
1
1.5
2

Figure 12

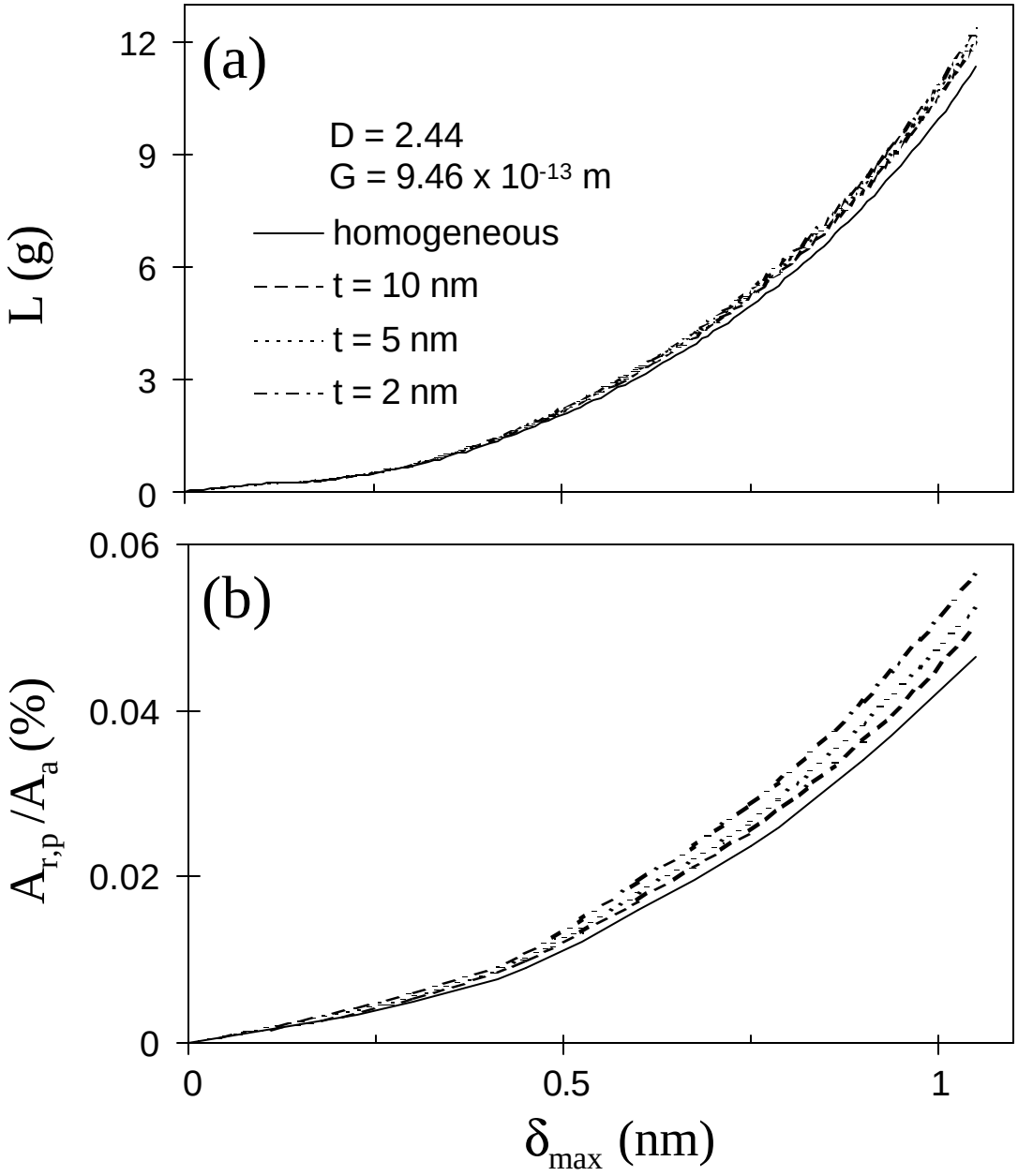
(a)
D = 2.44
G = 9.46 x 10-13 m
homogeneous
t = 10 nm
t = 5 nm
t = 2 nm
L (g)
12
9
6
3
0
(b)
Ar,p /Aa (%)
0.06
0.04
0.02
0
0
0.5
1
δmax (nm)

Figure 13

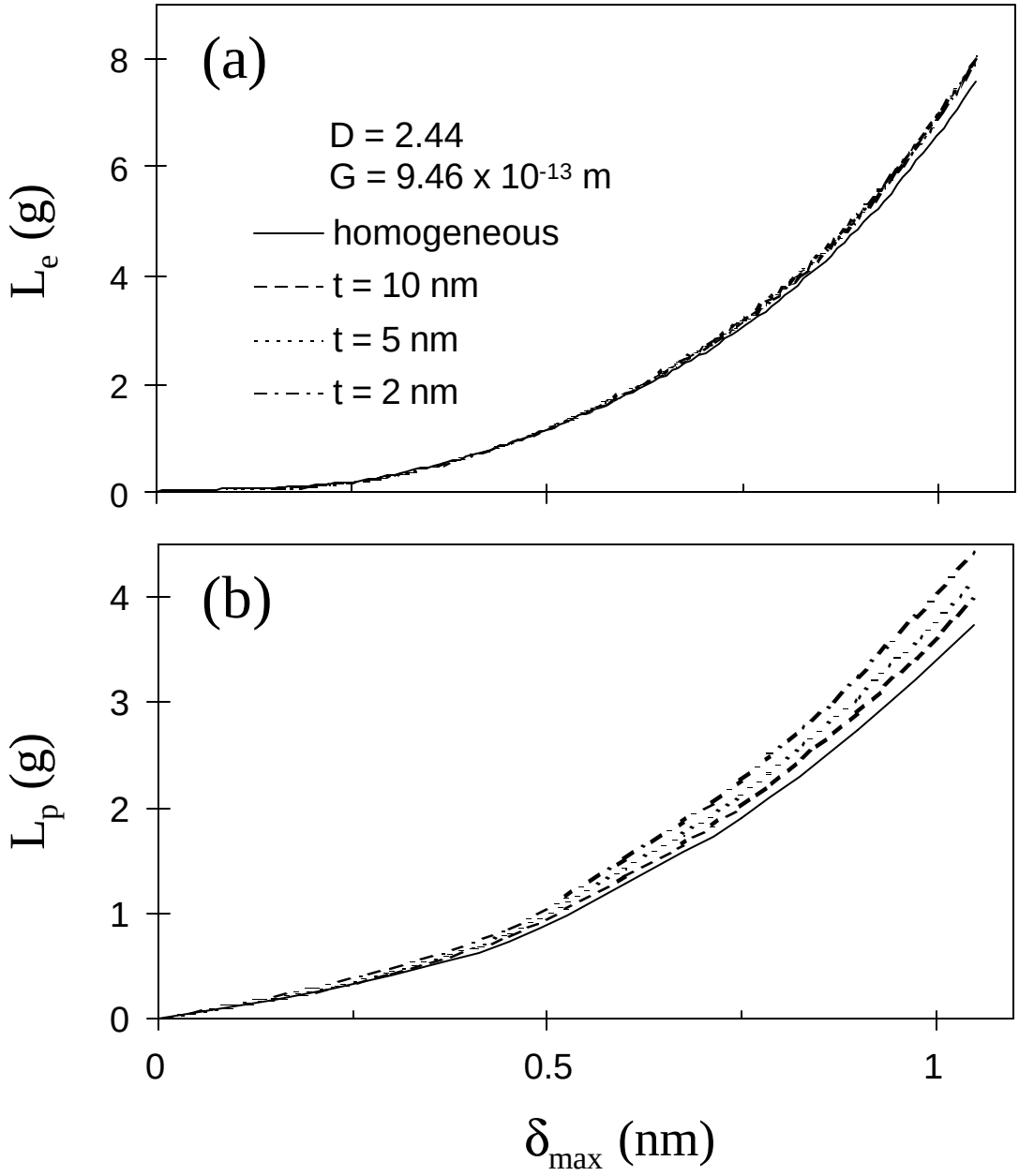
(a)
D = 2.44
G = 9.46 x 10-13 m
homogeneous
t = 10 nm
t = 5 nm
t = 2 nm
Le (g)
0
2
4
6
8
(b)
Lp (g)
0
1
2
3
4
0
0.5
1
δmax (nm)

Figure 14